Overall Loss Compensation and Optimization Control in Single-Stage Inductive Power Transfer Converter Delivering Constant Power

Fei Xu, *Student Member, IEEE*, Siu-Chung Wong, *Senior Member, IEEE*, and Chi K. Tse, *Fellow, IEEE*

***Abstract*—A typical battery charging process consists of a constant-current (CC) charging phase which is followed and completed by a constant-voltage charging phase. Moreover, replacing the CC charging by constant-power (CP) charging can eliminate thermal problems and enhance the cycle life of the battery. This work aims to maximize the system efficiency of a single-stage inductive power transfer (IPT) charger by minimizing the overall losses using a CP charging scheme. The single-stage CP IPT charger employs series-series compensation and adopts an active rectifier on the secondary side. Based on a time-domain model, the conditions of zero voltage switching (ZVS) and minimum circulating reactive power are derived. Then, the power losses in the magnetic coupler, inverter and active rectifier are analyzed and optimized under CP output condition. Combining the conditions of ZVS, minimum circulating reactive power, and minimum overall losses, we propose a novel optimal control strategy to maintain CP output and maximum efficiency throughout the charging process. In addition, the proportional integral controller is not needed. Finally, a 120-W experimental prototype is built to verify the performance of the proposed control strategy. Experimental results demonstrate high precision CP output and an efficiency of around 87.5% for the proposed single-stage inductive power transfer battery charger.**

***Index Terms*—Battery charging, conduction losses, constant power (CP), inductive power transfer (IPT), maximum efficiency, zero voltage soft switching.**

I. Introduction

INDUCTIVE power transfer (IPT) is a near field wireless power transmission technology, transferring power in a short distance by inductive coupling via magnetic fields. IPT has been widely applied for wireless battery charging with power rating ranging from several watts to hundreds of kilowatts. It has been found applications in portable electric devices [1]–[3], biomedical implants [4], [5], metro rail transit [6], [7], and electric vehicles (EV) [8]–[10].

Manuscript received February 23, 2021; revised May 24, 2021; accepted July 15, 2021. Date of publication July 26, 2021; date of current version September 16, 2021. This work was supported by in part by Hong Kong GRF under Grant 152096/17E and in part by RGC Theme-based Research Scheme under Grant T23-701-20-R. Recommended for publication by Associate Editor T. Mishima. *(Corresponding author: Fei Xu.)*

Fei Xu and Siu-Chung Wong are with the Department of Electronic and Information Engineering, The Hong Kong Polytechnic University, Kowloon, Hong Kong (e-mail: feifly.xu@connect.polyu.hk; enscwong@polyu.edu.hk).

Chi K. Tse is with the Electrical Engineering, City University of Hong Kong, Kowloon, Hong Kong (e-mail: cktse@ieee.org).

Color versions of one or more figures in this article are available at https://doi.org/10.1109/TPEL.2021.3098914.

Digital Object Identifier 10.1109/TPEL.2021.3098914

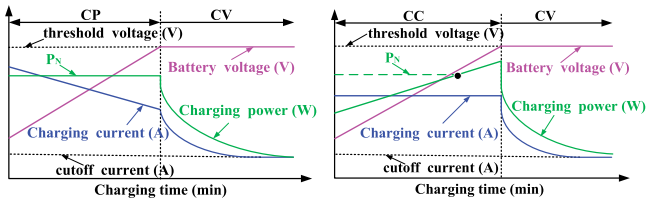

Fig. 1. Comparison of battery charging profiles. (a) CP–CV charging. (b) CC–CV charging.

IPT wireless chargers have been optimized for system efficiency and control with minimal wireless feedback signal between the secondary and the primary circuits. Typical charging modes including constant current (CC) and constant voltage (CV) outputs have been designed for efficient battery charging satisfying the typical CC–CV charging profile with minimal wireless feedback data bandwidth [11], [12]. However, such standard design is not efficiency-optimized when the battery as a load deviates from the optimal load resistance of the IPT converter during the charging process. Efficiency optimization may be achieved by using a multistage design with extra front-side and load-side converters for maintaining the necessary impedance matching that keeps the IPT converter at optimal efficiency [13]–[15].

The multistage IPT charger requires additional converters, which would incur extra losses in the IPT system. We can eliminate the front-side and load-side converters by an H-bridge inverter and an active rectifier which achieve the necessary input power control and output regulation. In such a design, the H-bridge inverter and the active rectifier must permit soft switching to enhance efficiency. Some previous works have performed impedance matching without considering switching losses from the H-bridge inverter and the active rectifier [16]–[19]. Moreover, when soft switching and frequency modulation are used to achieve maximum efficiency tracking [20], the resulting reactive circulating power becomes large and the VA ratings are high.

Constant-power (CP) mode charging has been found to benefit from better cycle life of the battery due to the inherent reduction in the charging current by the end of this charging phase [21] and being free from thermal problems [22], which is an alternative of CC mode charging. A comparison of CP–CV and CC–CV charging profiles is shown in Fig. 1. The charging process begins with CP or CC mode charging until the threshold voltage is

TABLE I
DESIRABLE CHARACTERISTICS OF AN IPT BATTERY CHARGER

Desirable characteristics	[16]	[19]	[20]	[22]
No additional dc-dc converter	√	√	√	×
ZVS for all MOSFETs	×	×	√	√
No frequency modulation	√	√	×	√
Small Circulating power	√	√	×	√
Without PI control	×	×	√	×
Overall loss optimization	×	×	×	×
Fast charging speed	√	×	×	√

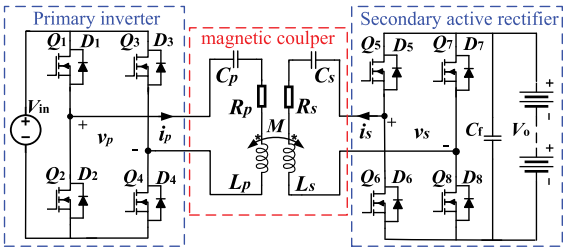

Fig. 2. Single-stage series-series compensated IPT battery charger.

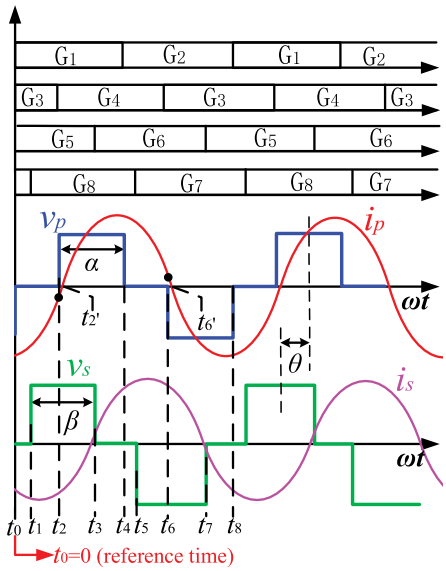

Fig. 3. Control signals and operating waveforms.

reached. The charging process continues with the CV mode to top up the state of charge (SOC) until the charging current falls to a predetermined cutoff value. It can be observed that during CP mode charging, the charging current decreases automatically as the battery voltage increases. However, during CC mode charging, the charging power starts at its minimum, increases proportionally to the battery voltage, and ends at its maximum. Obviously, compared with CC–CV charging profile, the CP–CV charging profile is suitable for designing faster IPT chargers. The optimization of an IPT charger with CP output can be implemented with an adaptive secondary-side series compensation by using an active variable capacitor [22]. However, the active capacitor being a switching mode converter increases the overall losses of the IPT system and operating the active capacitor to achieve load matching would increase the control complexity.

Moreover, most efficiency optimization models [12]–[20] are based on a linear equivalent model of the magnetic coupler of the IPT converter, ignoring the losses due to nonlinearity of the converter's operation including conduction loss in switches and diodes, hard switching loss of switches, and reverse recovery loss of diodes. The discrepancy between conventional loss models and experimental measurement has been well recognized [22]. A summary of merits of an IPT battery charger adopting an active rectifier developed is presented in Table I. It will be desirable to develop an IPT battery charger that has all the merits of no extra dc–dc converter, soft switching of the inverter and active rectifier circuits, no frequency modulation, small circulating reactive power, fast charging speed, and overall loss optimization. This article attempts to design a wireless fast battery charger adopting the CP–CV charging profile with all the desirable features shown in Table I, and using a single-stage series-series compensated IPT converter as shown in Fig. 2. In addition, compared with the CP IPT chargers in [22], our proposed optimized efficiency strategy can eliminate the proportional-integral (PI) controller using power perturbation and observation (P&O) strategy. The resulting design saves cost and alleviates stability problems.

The rest of this article is organized as follows. In Section II, a conventional equivalent model of the magnetic coupler of the IPT charger is briefly reviewed. In Section III, the conditions of zero voltage switching (ZVS) and minimum circulating reactive power are analyzed. In Section IV, the overall losses in the IPT system is analyzed and the condition of minimum overall losses is found. In Section V, an optimal control strategy for achieving ZVS, minimum circulating reactive power and minimum overall losses is derived. The control strategy is implemented and verified by an experiment prototype, which is presented in Section VI. Finally, Section VII concludes this article.

II. TIME-DOMAIN MODEL

A. System Structure and Control Angles

Fig. 2 shows a typical single-stage IPT charger. For ease of reference, subscripts p and s denote parameters in the primary and secondary sides, respectively. The magnetic coupler has self-inductances L_p with resistance R_p and L_s with resistance R_s, and mutual inductance M. The coupling coefficient is given by $k = \frac{M}{\sqrt{L_p L_s}}$. The series-series compensation capacitors C_p and C_s are driven by an inverter with a primary voltage v_p and an active rectifier with a secondary voltage v_s.

The inverter is fed by a dc voltage V_{in} and contains an H-bridge circuit with power devices Q_1 to Q_4, generating a high-frequency voltage v_p. The active rectifier generates output dc voltage V_o and the H-bridge with power devices Q_5 to Q_8 generates a high-frequency voltage v_s. Here, Q_1 to Q_8 are MOSFETs and D_1 to D_8 are the respective body diodes.

All power devices, Q_1 to Q_8, are driven by control signals G_1 to G_8. Fig. 3 shows the steady-state operating waveforms v_p, v_s, i_p, and i_s, with power switches achieving ZVS for the desired power flow as a battery charger. Control signals G_1 and G_2

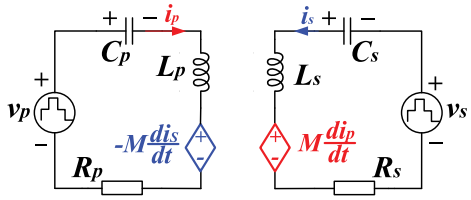

Fig. 4. Equivalent circuit of the magnetic coupler of Fig. 2.

are complementary square waveforms with a duty cycle slightly less than 50 percent to ensure the presence of a dead time that prevents simultaneous turn-ON of Q_1 and Q_2. This arrangement also applies to other transistor pairs (Q_3, Q_4), (Q_5, Q_6), and (Q_7, Q_8). The relative phase shift of transistor pairs (Q_1, Q_2) and (Q_3, Q_4) gives conduction angle $\alpha \in [0, \pi]$ which defines the duration of positive and negative voltages of v_p within one period. Similarly, the conduction angle $\beta \in [0, \pi]$ defines the duration of positive and negative voltages of v_s within one period. The relative phase angle $\theta \in [0, \pi/2]$ of v_p and v_s can be controlled by the relative phase of transistor pairs (Q_1, Q_2) and (Q_5, Q_6). The time sequence $\{t_0, \ldots, t_7\}$ is the turn-ON times of one of the eight power switches within a switching period that will be used together with the current waveforms i_p and i_s for ensuring ZVS of all transistors. Also, $t_0 = 0$ is set as time reference point of the system time-domain model; and t_2' and t_6' are the instants corresponding to $i_p = 0$ in rise and decline trends, respectively. The switching frequency is designed as usual at

$$\omega = \frac{1}{\sqrt{L_p C_p}} = \frac{1}{\sqrt{L_s C_s}}. \tag{1}$$

B. Output Power and Control Angles

An equivalent circuit of the magnetic coupler is shown in Fig. 4 [23]–[26]. The voltage waveforms of v_p and v_s are three-level square waves. Setting $t_0 = 0$ as the reference time point, the time-domain expressions of v_p and v_s can be approximated as the fundamental sinusoidal component for this high Q-circuit, i.e.,

$$v_p(t) = \frac{4}{\pi} V_{\text{in}} \cos\left(\omega t + \frac{\alpha}{2} - \pi\right) \sin\left(\frac{\alpha}{2}\right) \tag{2}$$

$$v_s(t) = \frac{4}{\pi} V_o \cos\left(\omega t + \frac{\alpha}{2} - \pi + \theta\right) \sin\left(\frac{\beta}{2}\right). \tag{3}$$

Applying Kirchhoff's Voltage Law (KVL) gives

$$i_p(t) R_p + L_p \frac{di_p(t)}{dt} + v_{C_p}(t) + M \frac{di_s(t)}{dt} = v_p(t) \tag{4}$$

$$i_s(t) R_s + L_s \frac{di_s(t)}{dt} + v_{C_s}(t) - M \frac{di_p(t)}{dt} = -v_s(t). \tag{5}$$

At resonance, the sum of the voltages across C_p and L_p is zero, and likewise for C_s and L_s. Thus, (4) and (5) can be approximated as

$$i_p(t) = \frac{v_p(t) - M \frac{di_s(t)}{dt}}{R_p} \tag{6}$$

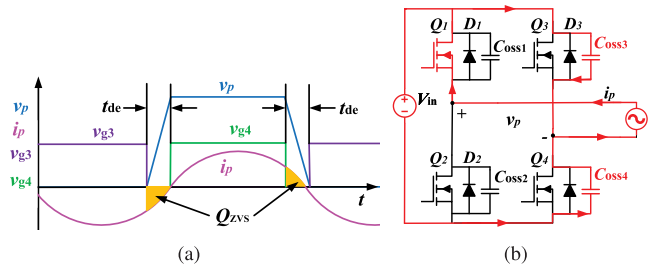

Fig. 5. ZVS technique for Q_3 and Q_4. (a) Operating waveforms for soft switching operation of Q_4 at t_2 and Q_3 at t_6. (b) Equivalent circuit just after Q_3 being turned OFF at t_2. Transistor Q_4 will be turned ON after the dead time t_{de}, i.e., at $t_2 + t_{\text{de}}$ and before i_p changes polarity. Dead time t_{de} should be designed to guarantee capacitor C_{oss3} being fully charged, capacitor C_{oss4} being fully discharged and the body diode of Q_4 being turned ON.

$$i_s(t) = \frac{M \frac{di_p(t)}{dt} - v_s(t)}{R_s}. \tag{7}$$

Substituting $v_p(t)$ in (2) and $v_s(t)$ in (3) into (6) and (7), and using $\omega M \gg R_s$ and $\omega^2 M^2 \gg R_p R_s$ for this high-Q circuit, we obtain

$$i_p(\vartheta) = \frac{4V_o}{\pi} \frac{\sin(\frac{\beta}{2}) \sin(\vartheta + \frac{\alpha}{2} - \pi + \theta)}{\omega M} \tag{8}$$

$$i_s(\vartheta) = \frac{4V_{\text{in}}}{\pi} \frac{\sin(\frac{\alpha}{2}) \sin(\vartheta + \frac{\alpha}{2} - \pi)}{\omega M} \tag{9}$$

where $\vartheta = \omega t$. During the battery charging process, we need to maintain CP output. The transmission power for this approximated lossless system can be expressed as

$$P = \frac{1}{2\pi} \int_0^{2\pi} v_p(\vartheta) i_p(\vartheta) d\vartheta. \tag{10}$$

Substituting $i_p(\vartheta)$ and $v_p(\vartheta)$ into the above equation, we obtain

$$P = P_M \sin\left(\frac{\alpha}{2}\right) \sin\left(\frac{\beta}{2}\right) \sin(\theta) \tag{11}$$

where $P_M = \frac{8 V_{\text{in}} V_o}{\pi^2 \omega M}$ is the maximum power output. The output power can be controlled monotonically by the control angles $\alpha \in [0, \pi]$, $\beta \in [0, \pi]$, and $\theta \in [0, \pi/2]$.

III. Conditions for ZVS and Minimum Circulating Reactive Power

To reduce the losses from the inverter and active rectifier, the conditions for ZVS should be maintained. Before a MOSFET turning ON, a minimum current $I_{\min}$ is needed to charge/discharge of the parasitic output capacitance C_{oss} of MOSFETs during dead time t_{de} as shown in Fig. 5(a), where the integral of i_p during t_{de} is denoted as Q_{ZVS}. The ZVS of Q_4 can be achieved when Q_{ZVS} is sufficient to charge C_{oss3} from 0 V to V_{in} and discharge C_{oss4} from V_{in} to 0 V, i.e.,

$$Q_{\text{ZVS}} = \int_0^{t_{\text{de}}} i_p(t) dt \geq \int_0^{V_{\text{in}}} (C_{\text{oss3}} + C_{\text{oss4}}) dv. \tag{12}$$

To determine $I_{\min}$ and the minimum dead time $t_{\text{de-min}}$ required by the ZVS, the waveform of i_p during the dead time is expressed as a piece-wise sine wave. Therefore, according to (12) and the

equivalent circuit shown in Fig. 5(b), $I_{\min}$ and $t_{\mathrm{de-min}}$ can be calculated from [27], i.e.,

$$I_{\min} = \frac{4V_o \sin\frac{\beta}{2}}{\pi\omega M}\sin\left(\arccos(1-X/2)\right) \approx \frac{4V_o \sin\frac{\beta}{2}}{\pi\omega M}\sin(\pi\sqrt{X}) \tag{13}$$

$$t_{\mathrm{de-min}} = \frac{T_s}{2}\sqrt{X} \tag{14}$$

where $X = \frac{V_{\mathrm{in}}(C_{\mathrm{oss1}}+C_{\mathrm{oss2}})\omega M \sin\frac{\beta}{2}}{V_o T_s}$ and $T_s = 2\pi/\omega$ is the switching period of the primary inverter and secondary active rectifier. The same condition applies to all other transistors. However, as transistors Q_1 and Q_2 switch at a much higher current level, the condition is automatically satisfied. Then, the conditions of ZVS in primary side are

$$\begin{cases} i_p(t_0) < -I_{\min} \\ i_p(t_2) < -I_{\min} \\ i_p(t_4) > I_{\min} \\ i_p(t_6) > I_{\min}. \end{cases} \tag{15}$$

Here t_0, t_2, t_4, and t_6 are turn-ON times of Q_1, Q_4, Q_2, and Q_3, respectively. Using odd symmetries of $i_p(t_0) = -i_p(t_4)$ and $i_p(t_2) = -i_p(t_6)$, as shown in Fig. 3, the ZVS conditions of the primary side can be simplified to

$$\begin{cases} i_p(t_0) < -I_{\min} \\ i_p(t_2) < -I_{\min}. \end{cases} \tag{16}$$

According to the current waveforms shown in Fig. 3, $i_p(t_0) < i_p(t_2)$ is satisfied automatically. Thus, the above inequality is simply

$$i_p(t_2) < -I_{\min}. \tag{17}$$

Similarly, ZVS of secondary switches requires $i_s(t_3) > I_{\min}$. Hence, from (17), the conditions of ZVS in both sides are

$$\begin{cases} i_p(t_2) < -I_{\min} \\ i_s(t_3) > I_{\min}. \end{cases} \tag{18}$$

However, if $i_p(t_2)$ is far from $-I_{\min}$, the long duration of v_p and i_p being in opposite polarity would create excessive circulating reactive power in the system, denoted as P_{cr}. The reactive power will lead to more hard turn-OFF loss in the MOSFETs as well as reverse recovery loss in body diodes. This increases the VA rating of the supply source. As a result, the stress on power devices will increase and the system efficiency will decrease. In one period, there are two stages, namely, $(t_2 - t_2')$ and $(t_6 - t_6')$, where reactive power circulates, as shown in Fig. 3. The equivalent circuits of current flow path are shown in Fig. 6. Generally, this reactive power loss can be mitigated by designing α, β, and θ to control $i_p(t_2) = -I_{\min}$, such that $|P_{\mathrm{cr}}|$ is just sufficient to discharge all parasitic capacitances of the power switches. According to the specification of the IPT charger and the value of C_{oss} of MOSFETs provided by the manufacturer's datasheet, the calculated $I_{\min}$ and $t_{\mathrm{de-min}}$ are 0.4205 A and 171.9 ns, respectively. Accounting for the loss in the calculation, design margins of $I_{\min} = 1$ A and $t_{\mathrm{de-min}} = 200$ ns are adopted here.

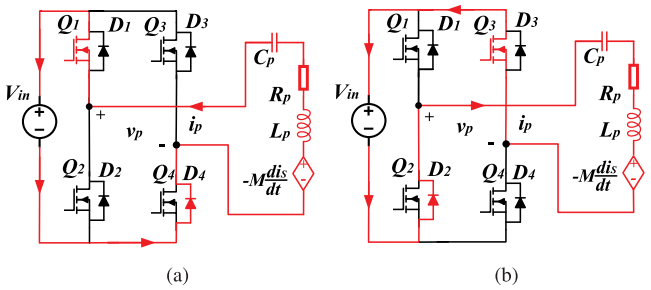

Fig. 6. Two periods of circulating power. (a) $t_2 - t_2'$. (b) $t_6 - t_6'$.

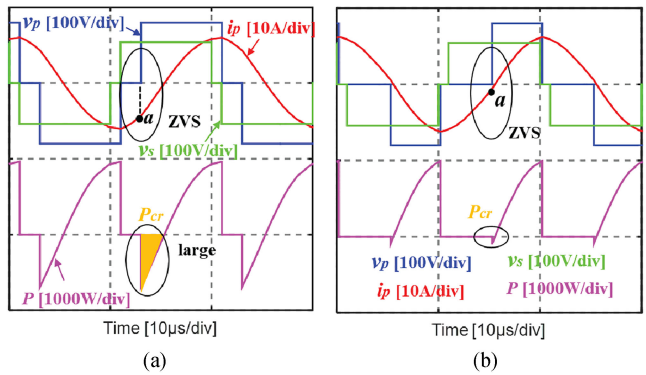

Fig. 7. Simulated waveforms. (a) $(\alpha, \beta, \theta) = (0.78\pi, 0.90\pi, 0.17\pi)$. (b) $(\alpha, \beta, \theta) = (0.49\pi, 0.90\pi, 0.24\pi)$. $P_N = 120$ W. Time base is 10 μs/div.

TABLE II
SIMULATION PARAMETERS

Parameters	Symbols	Values
Rated charging power	P_N	120 W
Battery charging voltage	$[V_{\min}, V_{\max}]$	[55 V, 78 V]
Input voltage	V_{in}	80 V
Switching frequency	f	50 kHz
Self inductance	L_p, L_s	118 μH, 175 μH
Coupling coefficient	k	0.252
Coil resistances	R_p, R_s	0.21 Ω, 0.254 Ω
Compensation capacitances	C_p, C_s	86 nF, 58 nF

Fig. 7 shows the simulation results for two different combinations of α, β, and θ, with $P_N = 120$ W and $I_{\min} = 1$ A. Fig. 7(a) shows ZVS at point a (i.e., $i_p(t_2) < -1$ A) with a large circulating reactive power P_{cr}, and Fig. 7(b) shows an optimized result of ZVS at point a (i.e., $I_{\min} = -1$ A) with small circulating reactive power P_{cr}. The simulation parameters given in Table II will be used for the rest of this article, unless specified otherwise.

By controlling α, β, and θ to achieve $i_p(t_2) = -I_{\min}$, both ZVS and a small P_{cr} can be achieved. In addition, for the secondary side, $i_p(t_3) > I_{\min}$ should be satisfied in order to ensure ZVS. From Fig. 3, we can get $\vartheta_2 = \omega t_2 = \pi - \alpha$ and $\vartheta_3 = \omega t_3 = \pi - \frac{\alpha}{2} - \theta + \frac{\beta}{2}$. Substituting ϑ_2 and ϑ_3 into (8) and (9), respectively, the conditions for achieving ZVS and minimum circulating power are

$$i_p(t_2) = \frac{4V_o}{\pi}\frac{\sin(\frac{\beta}{2})\sin(-\frac{\alpha}{2}+\theta)}{\omega M} = -I_{\min}, \text{ and} \tag{19}$$

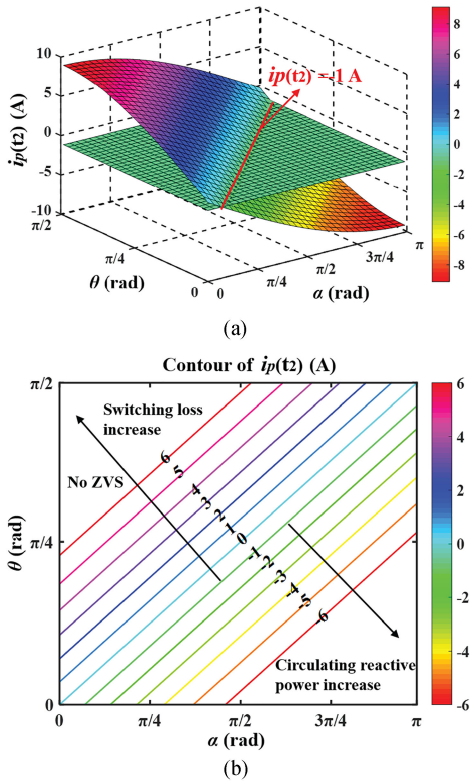

Fig. 8. Simulation of $i_p(t_2)$ versus α and θ. (a) 3D plot with $V_o = 78$ V. (b) Contour of $i_p(t_2)$ with $V_o = 78$ V.

$$i_s(t_3) = \frac{4V_{\text{in}}}{\pi}\frac{\sin(\frac{\alpha}{2})\sin(\frac{\beta}{2}-\theta)}{\omega M} \geq I_{\min}. \tag{20}$$

Normally, V_{in} is constant, and we can adjust this value to suit the application. The battery voltage, V_o, would increase during CP charging until the predetermined threshold voltage $V_{\max}$ is attained, as shown in Fig. 1. Here, since $(V_o \sin\frac{\beta}{2})/(V_{\text{in}} \sin\frac{\alpha}{2}) = 1$ (as shown in Section IV-C), and $V_{\text{in}} \geq V_{\max}$, we have $\beta \geq \alpha$, and thus, (19) implies (20). Therefore, we only need to focus on (19).

According to (19), we can plot $i_p(t_2)$ versus α and θ, as shown in Fig. 8. For a certain value of $I_{\min}$, say 1 A, possible solutions of α and θ are linearly related. By modulating α and θ to maintain $i_p(t_2) = -I_{\min}$, we can achieve ZVS and minimum circulating reactive power. If $i_p(t_2) > -I_{\min}$, ZVS cannot be ensured, and if $i_p(t_2) < -I_{\min}$, the circulating large reactive power becomes significant.

IV. Loss Analysis and Optimization

Once ZVS and minimum circulating reactive power have been achieved, the overall efficiency of the IPT system can be maximized by minimizing the power losses in the inverter, the magnetic coupler, and the active rectifier. Impedance matching for achieving maximum efficiency can be implemented by using the equivalent magnetic coupler shown in Fig. 4 [13]–[15], [17]. However, the losses in the inverter and the active rectifier include hard turn-OFF loss of MOSFETs, conduction loss of MOSFETs and reverse recovery loss of diodes, which are not optimized. In this section, we try to control rms current values of the primary and secondary sides to optimize the overall losses by modulating α, β, and θ.

A. Impedance Matching of the Magnetic Coupler

Referring to the equivalent circuit shown in Fig. 4, the resistive power loss in the magnetic coupler can be expressed as

$$P_{\text{coil-loss}} = I_p^2 R_p + I_s^2 R_s \tag{21}$$

where I_p and I_s are rms values of i_p and i_s, respectively. Using (8) and (9), we have

$$I_p = \sqrt{\frac{1}{\pi}\int_0^{\pi} i_p(t)^2\, d(\omega t)} = \frac{2\sqrt{2}V_o}{\pi\omega M}\sin\frac{\beta}{2}, \text{ and} \tag{22}$$

$$I_s = \sqrt{\frac{1}{\pi}\int_0^{\pi} i_s(t)^2\, d(\omega t)} = \frac{2\sqrt{2}V_{\text{in}}}{\pi\omega M}\sin\frac{\alpha}{2}. \tag{23}$$

The efficiency of this magnetic coupler can be expressed as

$$\eta_{\text{coil}} = \frac{P}{P + P_{\text{coil-loss}}}. \tag{24}$$

Substituting (11), (21), (22), and (23) into (24), we obtain

$$\eta_{\text{coil}} = \frac{\omega M \sin\theta}{\omega M \sin\theta + KR_p + \frac{1}{K}R_s} \tag{25}$$

where

$$K = \frac{V_o \sin\frac{\beta}{2}}{V_{\text{in}} \sin\frac{\alpha}{2}} = \frac{I_p}{I_s}. \tag{26}$$

The efficiency is maximized at $\theta = \pi/2$. For the other two control parameters, the maximum efficiency can be calculated by solving

$$\frac{\partial \eta_{\text{coil}}}{\partial K} = 0 \tag{27}$$

which gives

$$K = \frac{I_p}{I_s} = \sqrt{\frac{R_s}{R_p}}. \tag{28}$$

This implies that $I_p^2 R_p = I_s^2 R_s$ for an even distribution of losses in the primary and secondary sides.

Using parameters shown in Table I as an illustration, Fig. 9 shows the power loss $P_{\text{coil-loss}}$ of the equivalent circuit shown in Fig. 4 versus the current ratio I_p/I_s. This verifies that $P_{\text{coil-loss}}$ is minimized when $I_p/I_s = \sqrt{0.254/0.21} = 1.1$. However, ZVS cannot be achieved by impedance matching control with $\theta = 0.5\pi$. Power devices Q_4 and Q_5 cannot achieve ZVS, because $i_p(t_2) = \frac{4V_o}{\pi}\frac{\sin(\frac{\beta}{2})\sin(-\frac{\alpha}{2}+\theta)}{\omega M} > 0$ with $\theta = 0.5\pi$. Thus, for the proposed IPT system, the minimum magnetic coupler loss cannot be achieved if ZVS is to be maintained for the power devices.

B. Losses in Inverter and Active Rectifier

As shown earlier in Fig. 3, the current freewheeling paths are (D_1, Q_3) in interval $t_0 - t_2$ and (D_2, Q_4) in interval $t_4 - t_6$ [17].

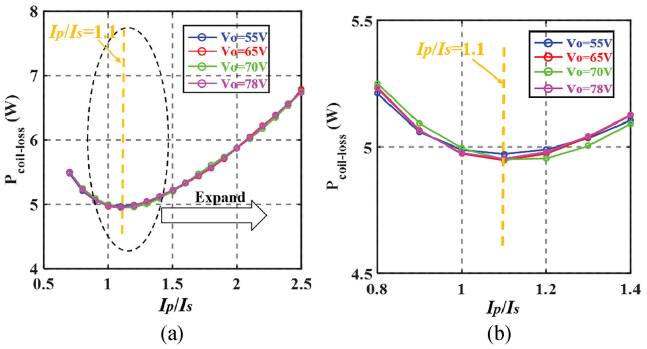

Fig. 9. Magnetic coupler circuit simulation of power loss $P_{\text{coil-loss}}$ versus current ratio I_p/I_s with $\sqrt{R_s/R_p} \approx 1.1$. (a) I_p/I_s ranges from 0.5 to 2.5. (b) Enlarged view.

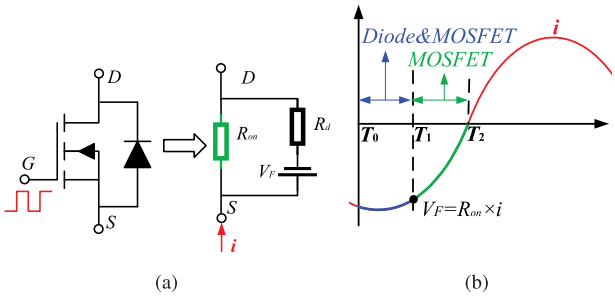

Fig. 10. (a) Equivalent model of a conducting MOSFET. (b) Two situations of current flow.

TABLE III
OPTIMAL SOLUTIONS FOR DIFFERENT VALUES OF K WITH $V_o = 78$ V

K	0.8	0.9	1	1.1	1.2
α_K	0.542π	0.519π	0.500π	0.483π	0.469π
β_K	0.423π	0.469π	0.516π	0.566π	0.620π
θ_K	0.197π	0.186π	0.176π	0.168π	0.161π

Moreover, during intervals $t_0 - t_2$ and $t_4 - t_6$, the freewheeling paths could also be (Q_1, Q_3) and (Q_2, Q_4), which are determined by the current values. When a MOSFET turns ON, it is equivalent to a constant ON-state resistance R_{on} and the body diode is equivalent to a forward voltage source V_F connected in series with a small resistance R_d, as shown in Fig. 10(a). From the equivalent circuit, we clearly see that when the value $R_{\text{on}} i > V_F$, current will flow in both MOSFET and diode, whereas when $R_{\text{on}} i < V_F$, current will only flow through the MOSFET, as shown in Fig. 10(b).

According to (8) and (9), the maximum value of i_p and i_s are $4V_{\max}/(\pi\omega M)$ and $4V_{\text{in}}/(\pi\omega M)$, respectively. Using the experimental parameters listed in Table IV, the peak values of i_P and i_s are 8.75 and 8.97 A, respectively. The type of MOSFETs used is IPP65R045. Looking up the data sheet, we know the body diode forward voltage V_{SD} is about 0.9 V and the MOSFET's ON-resistance is 45 mΩ. The peak values of $R_{on} i_p$ and $R_{on} i_s$ are both less than V_{SD}. Therefore, during $t_0 - t_2$ and $t_4 - t_6$, the current freewheeling paths are (Q_1, Q_3) and (Q_2, Q_4), respectively. The different kinds of losses in the inverter and the active rectifier are calculated as follows.

TABLE IV
PARAMETERS OF EXPERIMENTAL PROTOTYPE

Parameters	Symbols	Values
Rated charging power	P_N	120 W
Battery charging voltage	V_o	55 V-78 V
Input voltage	V_{in}	80 V
Switching frequency	f	50 kHz
MOSFETs	$Q_1 - Q_8$	IPP65R045
Diode	$D_1 - D_8$	MBR20200
Dead Time	t_{de}	200ns
Self inductance	L_P, L_S	117.9 μH, 174.4 μH
Coupling coefficient	k	0.252
Coil resistances	R_P, R_S	0.21 Ω, 0.254 Ω
Compensation capacitances	C_P, C_S	85.99 nF, 58.15 nF

1) Conduction Loss of MOSFETs: When a MOSFET is turned ON, it is a constant on-resistance, and the loss can be calculated by

$$P_{\text{on},p} = I_p^2 \times 2R_{\text{on}} \tag{29}$$

$$P_{\text{on},s} = I_s^2 \times 2R_{\text{on}}. \tag{30}$$

Here, R_{on} is the equivalent on-resistance of the MOSFET, $P_{\text{on},p}$ and $P_{\text{on},s}$ are the conduction losses of the MOSFET in the primary and secondary sides, respectively.

2) Hard Turn-OFF Loss of MOSFETs: Since ZVS is guaranteed, the hard switching loss is the turn-OFF loss in MOSFETs. By symmetry, Q_1 and Q_2 are turned OFF with current $i_p(t_0)$, while Q_4 and Q_3 are turned OFF with current $I_{\min}$. Similarly, on the secondary side, Q_7 and Q_8 are turned OFF with current $i_s(t_1)$, and Q_5 and Q_6 are turned OFF with current $i_s(t_3)$. The overall turn-OFF loss can be calculated by

$$P_{\text{sw},p} = \frac{1}{T} V_{\text{in}} |I_{\min}| t_{\text{off}} + \frac{1}{T} V_{\text{in}} |i_p(t_0)| t_{\text{off}} \tag{31}$$

$$P_{\text{sw},s} = \frac{1}{T} V_o |i_s(t_1)| t_{\text{off}} + \frac{1}{T} V_o |i_s(t_3)| t_{\text{off}} \tag{32}$$

where t_{off} is the turn-OFF time of the MOSFET, which is approximately equal to the dead time t_{de}. In addition, we can see if we control $I_{\min}$ at turn-ON time of the MOSFET, as analyzed in Section III, the turn-OFF loss of MOSFETs can be minimized.

3) Diode Loss: As the conducting paths do not flow through the diodes during intervals $t_0 - t_2$ and $t_4 - t_6$, the conducting loss of diodes can be overlooked compared with the large reverse recovery loss. Fig. 11(a) shows the reverse recovery process of the body diode for MOSFET IPP65R045, and Fig. 11(b) shows the measured profile using a double pulse test with 5 A. The body diode has a long reverse recovery time t_{rr}, peak current I_{RRM}, and voltage V_{RRM}. The hatched area in Fig. 11(a) indicates the reverse recovery loss, which can be calculated as

$$P_{\text{re}} = P_{t_S} + P_{t_F} = \frac{V_F}{T} \int_0^{t_S} i_R dt + \frac{1}{T} \int_0^{t_F} i_R V_R dt$$

$$= V_F I_{\text{RRM}} \frac{t_S}{2T} + V_{\text{RRM}} I_{\text{RRM}} \frac{t_F}{4T}. \tag{33}$$

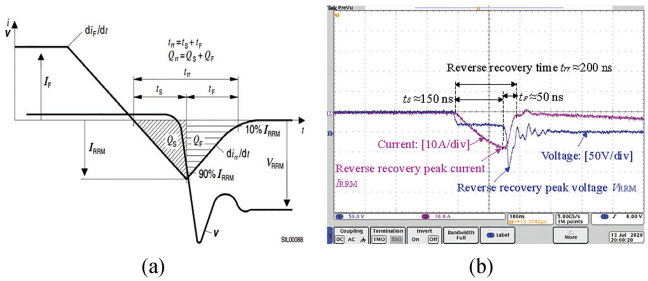

Fig. 11. (a) Reverse recovery process of body diode of MOSFET IPP65R045. (b) measured reverse recovery profile.

where t_S and t_F are duration of different stages of the reverse recovery time. The reverse recovery process occurs at each switching time when the current commutes from the body diode to the MOSFET. Using a double pulse test, the peak current and voltage can be measured with different values of switching current, as shown in Fig. 11(b), and the reverse recovery losses $P_{\mathrm{re},p}$ and $P_{\mathrm{re},s}$ can be evaluated.

The reverse recovery losses are $P_{\mathrm{re},p} = 2.60$ W and $P_{\mathrm{re},s} = 2.80$ W under $V_o = 55$ V, $I_{\min} = -1$ A and $K = 1$. The body diode does not work adequately as a freewheel diode for the IPT system because of the longer reverse recovery time and large peak current and voltage. Here, we parallel a Schottky barrier diode (SBD) to eliminate the reverse recovery loss to improve the system efficiency. The losses of the primary inverter and secondary active rectifier is the sum of all power consumed by MOSFETs and diodes, $P_{\text{converter-loss}} = P_{\mathrm{on},p} + P_{\mathrm{sw},p} + P_{\mathrm{on},s} + P_{\mathrm{sw},s}$.

C. Optimal RMS Current Ratio for ZVS and Minimum Overall Loss

As discussed in Section IV-A, the magnetic coupler loss $P_{\text{coil-loss}}$ is minimized when $I_p/I_s = \sqrt{R_s/R_p}$ since $P_{\text{converter-loss}}$ is also related to the rms currents of I_p and I_s. With the aim of minimizing the overall loss P_{loss}, under a set of constraints including the rated transmission power P_N, the minimum current $I_{\min}$ for ZVS, minimum circulating power, and the ratio of I_p/I_s, the optimal solution of I_p/I_s can be obtained by minimizing P_{loss}, i.e.,

$$\min\left(P_{\text{loss}}\left(\alpha,\beta,\theta\right)\right)$$
$$s.t.\begin{cases} P_N = \frac{8V_{\mathrm{n}}V_o}{\pi^2\omega M}\sin\frac{\alpha}{2}\sin\frac{\beta}{2}\sin\theta \\ i_p(t_2) = \frac{4V_o}{\pi}\frac{\sin(\frac{\beta}{2})\sin(-\frac{\alpha}{2}+\theta)}{\omega M} = I_{\min} \\ \frac{I_p}{I_s} = \frac{V_o\sin\frac{\beta}{2}}{V_{\mathrm{in}}\sin\frac{\alpha}{2}} = K \end{cases} \tag{34}$$

where $P_{\text{loss}} = P_{\text{coil-loss}} + P_{\text{converter-loss}}$, which is the sum of equations (21), (29), (30), (31), and (32). I_p and I_s are given in (22) and (23). The current points $i_p(t_0)$, $i_p(t_1)$, and $i_s(t_3)$ inside (31) and (32) are given by

$$\begin{cases} i_p(t_0) = \frac{4V_o}{\pi}\frac{\sin(\frac{\beta}{2})\sin(\frac{\alpha}{2}-\pi+\theta)}{\omega M} \\ i_s(t_1) = \frac{4V_{\mathrm{in}}}{\pi}\frac{\sin(\frac{\alpha}{2})\sin(-\frac{\beta}{2}+\theta)}{\omega M} \\ i_s(t_3) = \frac{4V_{\mathrm{in}}}{\pi}\frac{\sin(\frac{\alpha}{2})\sin(-\frac{3\beta}{2}+\theta)}{\omega M}. \end{cases} \tag{35}$$

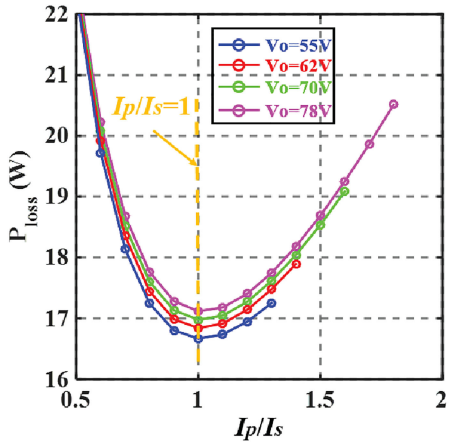

Fig. 12. Overall system losses P_{loss} versus I_p/I_s.

In this way, P_{loss} can be expressed as a function of α, β, and θ. Equation (34) can be solved numerically. The procedure is as follows. Given a value of K, a numerical solution (α_K, β_K, θ_K) for the value of P_{loss} in (34) is obtained. Using the parameters given in Table IV, some numerical solutions under different values of K with $V_o = 78$ V are listed in Table III. More solutions can also be found. Based on these numerical solutions, the optimal K corresponding to a minimum P_{loss} can be picked to control the IPT converter. As an intuitive illustration, we plot P_{loss} versus I_p/I_s, as shown in Fig. 12, for an optimal rms current ratio which achieves ZVS and minimum overall losses, i.e.,

$$K_{\text{optimal}} = \frac{I_p}{I_s} = 1. \tag{36}$$

V. Design Considerations

During the CP charging process, the battery voltage V_o would increase until the predetermined threshold voltage is reached. In order to keep the output power at the rated level P_N, we need to adjust α, β, or θ adaptively according to V_o. At the same time, the conditions for ZVS, minimum circulating reactive power, and minimum overall losses, given earlier in Section IV, should be achieved by controlling α, β, and θ.

A. Optimal Control Strategy

By setting $K = 1$ obtained in (36), the optimal solution of (α,β,θ) in (34) can be obtained. An approximate method can be adopted by the following three steps. Normally, $I_{\min} < -1$ A. Thus, $|\theta - \frac{\alpha}{2}| \approx 0$. The first step is to let $\theta = \alpha/2$ and substitute it into (34), i.e.,

$$\alpha' = 2\arcsin\left(\sqrt[3]{\frac{P_N\pi^2\omega M}{8V_{in}^2}}\right) \tag{37}$$

$$\theta' = \arcsin\left(\sqrt[3]{\frac{P_N\pi^2\omega M}{8V_{in}^2}}\right). \tag{38}$$

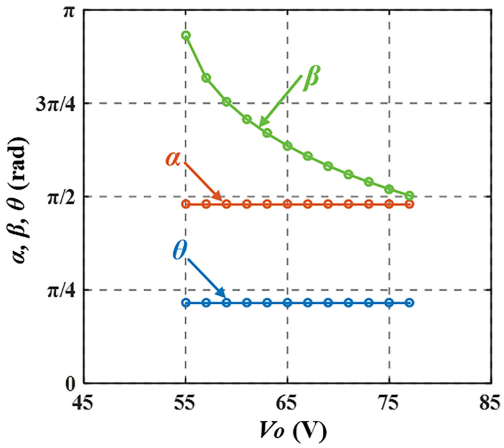

Fig. 13. α, β, and θ versus with battery voltage V_o.

Suppose $\sigma = |\theta - \alpha/2|$ is the difference between θ and $\alpha/2$ to make $I_{\min} = -1$ A. Then, θ is given by

$$\theta = \theta' - \sigma. \tag{39}$$

Finally, to find α and β that satisfy the rated power P_N, we put (39) into (34) again, giving

$$\alpha = 2\arcsin\left(\sqrt{\frac{P_N \pi^2 \omega M}{8 V_{in}^2 \sin\theta}}\right) \tag{40}$$

$$\beta = 2\arcsin\left(\sqrt{\frac{P_N \pi^2 \omega M}{8 V_o^2 \sin\theta}}\right). \tag{41}$$

Since P_N increases monotonically with α, β, and θ, this solution method can guarantee $\sigma \approx |\theta - \frac{\alpha}{2}|$, while maintaining $I_p/I_s = 1$ and constant P_N simultaneously.

B. Compensated Overall Losses

Traditional CP charging requires sampling the output current and voltage in order to obtain the output power. Then, a proportional-integral (PI) controller is used to regulate the output power constant [19]. The PI controller is used to compensate the system loss. In this article, as the system loss P_{loss} has been found accurately, the rated power P_N can be compensated with $P'_N = P_N + P_{\text{loss}}$ and we use P'_N to get the solutions for (α, β, θ). The variations of α, β, and θ with V_o are shown in Fig. 13. Here, $\sigma = 0.12$ rad, which can be adjusted adaptively according to system parameters. We see that β decreases as V_o increases, while α and θ are kept constant throughout the CP charging process. Due to the fixed α in the primary inverter and the fixed phase shift angle θ between the two sides, a synchronization signal is needed. Thus, we can simply store α and θ in microcontrollers on the primary and second sides, respectively.

The overall control diagram is shown in Fig. 14. The battery voltage V_o is sampled and sent to the secondary microcontroller. Meanwhile, based on V_o, the control signal of β can be calculated according to (41). During the CP charging process, we only need to adjust β to maintain constant output under any

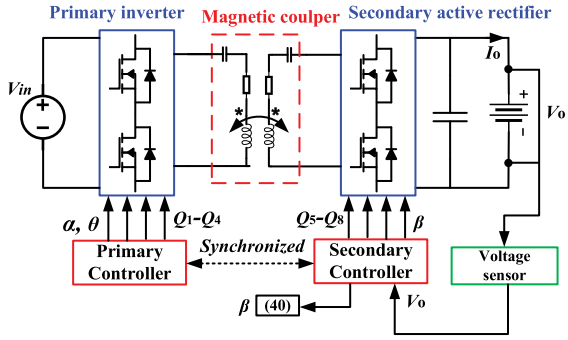

Fig. 14. Overall optimal control for maximum efficiency and CP charging.

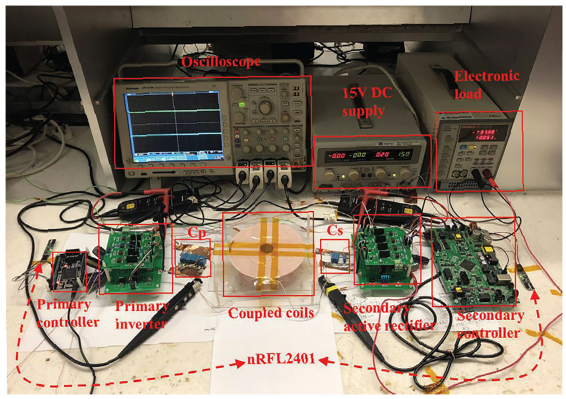

Fig. 15. Photograph of the experimental prototype.

variation of load resistance. The PI controller can be eliminated. Furthermore, the proposed control is free from any possible shift in optimal solution as the PI controller is no longer needed to adjust α, β, or θ continuously.

From Fig. 12, we see that P_{loss} varies very slightly from 16.7 to 17.2 W. Therefore, we may assume power loss being constant, e.g., 17 W, to compensate for the rated power. The rated power $P_N = 120$ W is adjusted to $P'_N = 137$ W in the design. Moreover, as the system loss has a relationship with V_o, we can adaptively set the compensated values for all other parameters according to V_o. Finally, considering the effect of temperature variation, we may include a thermal factor to further compensate for the change in the parameters for achieving optimized efficiency.

VI. Experimental Verification

An experimental prototype has been built, as shown in Fig. 15, to verify the analysis and efficiency performance in the charging process. Both primary and secondary sides use DSP TMS320F28335 as the microcontrollers. The wireless communication is linked by RF modules (nRF24L01). An electronic load (PRODIGIT3302) is used to emulate the battery. Based on the battery charging specifications, the range of output voltage V_o is 55–78 V in the CP charging process with the output power rated at 120 W, as given in Table II. The equivalent load resistance R_L can be calculated by $R_L = V_o^2/P_o$ and the range is from 25.2 to 50.7 Ω. All voltages and currents are recorded

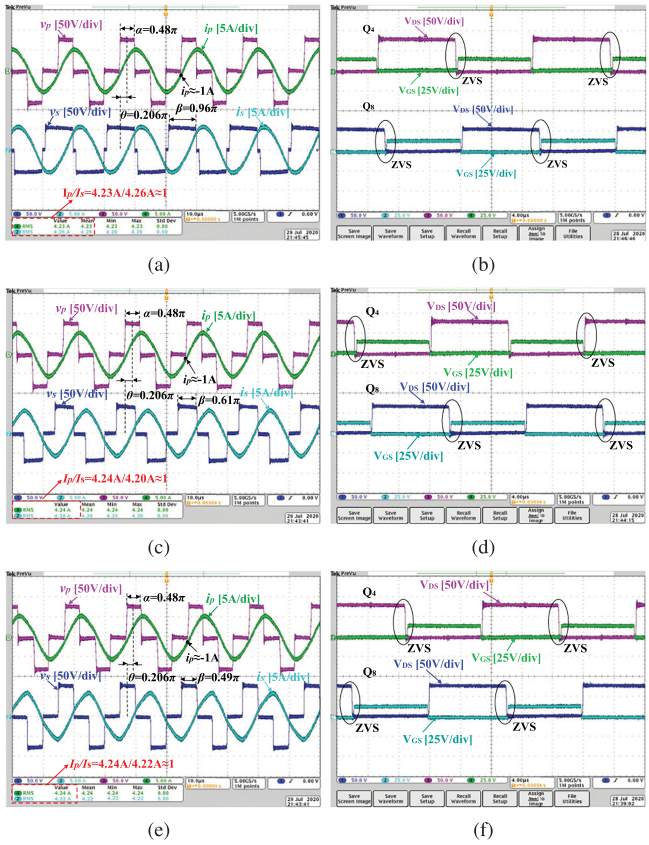

Fig. 16. (a), (c), and (e) show experimental steady-state operating waveforms of v_p, i_p, v_s, and i_s at start ($R_L = 25.2\Omega$), middle ($R_L = 37.4\Omega$), and end ($R_L = 50.7\Omega$) of CP charging process. (b), (d), and (f) show ZVS validation.

by a Tektronix DPO 4104 Oscilloscope. Powers and efficiency values were measured by a precision power scope YOKOGAWA PX8000. The other main parameters of the prototype are listed in Table IV.

A. Steady-State Waveforms

Fig. 16 shows the steady-state experimental waveforms at the start, middle, and end of the CP charging process. Comparing Fig. 16(a) with Fig. 16(c) and (e), we can see that the primary inverter's conduction angle α and phase shift angle θ are kept constant at 0.48π and 0.206π, and the conduction angle β in the secondary active rectifier decreases from 0.94π to 0.49π as the resistances increase. The rms current ratio remains unchanged with $I_p/I_s \approx 1$, which agrees with the analysis given in Section IV. In addition, as shown in Fig. 16(b), (d), and (f), when the drive signals V_{GS} turn ON Q_4 and Q_8, the drain source voltage V_{DS} is zero, validating the ZVS operation.

The primary current at turn-ON time of Q_4 is kept almost unchanged with $i_p(t_2) \approx -1$ A, corresponding to a very small circulating reactive power $P_{\rm cr}$. In order to examine $P_{\rm cr}$, we log the experimental data shown in Fig. 16(a) and (e) with MATLAB and replot them in Fig. 17. We verify the circulating reactive power $P_{\rm cr}$ being all very small, indicating that the system has achieved ZVS and minimum circulating reactive power simultaneously.

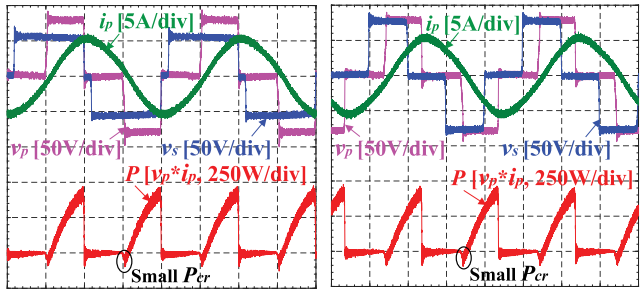

Fig. 17. Experimental waveforms of circulating reactive power at (a) start and (b) end of the CP charging process.

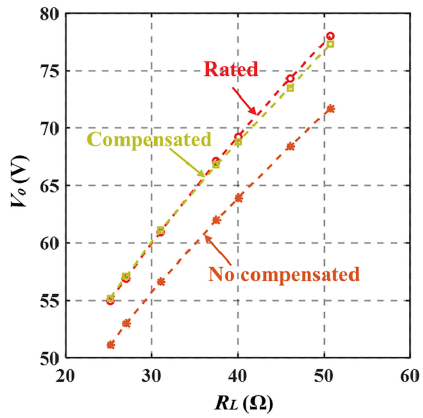

Fig. 18. Comparison of measured output voltage versus load resistance.

Fig. 19. Screen capture of power analyzer at (a) start and (b) end of the charging process.

B. Efficiencies and Losses

We took seven operating points along the CP charging process and compared the compensated and uncompensated system overall losses. The measured results of output voltage V_o and output power P_o are plotted in Fig. 18. We observe that the compensated system gives an output voltage close to the ideal rated value, whereas the uncompensated system gives a lower output voltage.

We used a precision power scope to measure the input power, output power, and efficiency of the system, and the results taken at the start and end of the CP charging are shown in Fig. 19. The overall system loss is 16.94 W at the start and 17.24 W at the end of the CP charging, which are consistent with the minimum system overall losses calculated in Section IV and

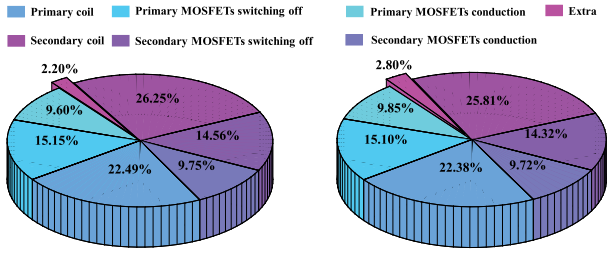

(a) (b)

Fig. 20. Power loss distribution of the proposed IPT charger at (a) start of charging process with $P_{\text{loss}} = 16.94\,\text{W}$ and (b) end of charging process with $P_{\text{loss}} = 17.24\,\text{W}$.

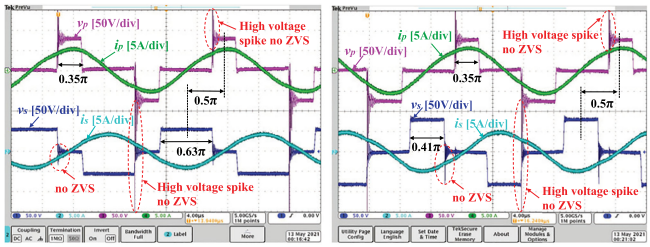

(a) (b)

Fig. 21. Experimental steady-state waveforms of v_p, i_p, v_s, and i_s under impedance matching condition of $K = 1.1$ and $\theta = 0.5\pi$ at (a) the start ($R_L = 25.2\,\Omega$) and (b) the end ($R_L = 50.7\,\Omega$) of CP mode charging.

shown in Fig. 12. The distribution of the different kinds of losses is shown in Fig. 20. The loss in the coupled coils accounts for 48.74% of the total loss in the start and 48.19% in the end of the CP charging. The conduction and turn-OFF losses have accounted for 19.35% and 29.71% of the overall losses with little variation throughout the CP charging process. The extra loss corresponds to diode conduction loss and the loss caused by harmonic components, which have been mostly ignored in previous studies. As we have discussed in Section IV-A, the impedance matching condition with $K = \sqrt{I_p/I_s} = 1.1$ and $\theta = 0.5\pi$ can achieve a global minimum conduction loss in the magnetic coupler. However, ZVS cannot be achieved. A comparison of our proposed optimal CP control strategy and the impedance matching should be considered. Fig. 21 shows the steady-state waveforms of impedance matching at the start and end of the CP charging. It can be observed that ZVS cannot be achieved, and the high voltage spikes and oscillations would incur a large switching loss. The measured system efficiencies are 80.6% and 80.3% at the start and end of the CP charging process, which are both lower than the 87.5% efficiency of our proposed optimal CP control.

C. Misalignment

Coil misalignment may occur due to the position variation of the primary and secondary coils. Stable output power and high efficiency should also be guaranteed under misaligned conditions. According to (39), (40), and (41), the optimal solution depends on the mutual inductance M. Thus, we need to estimate the mutual inductance in order to determine the optimal solution.

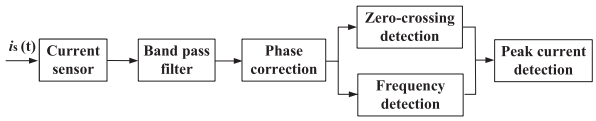

Fig. 22. Peak current detection method of the receiving coil.

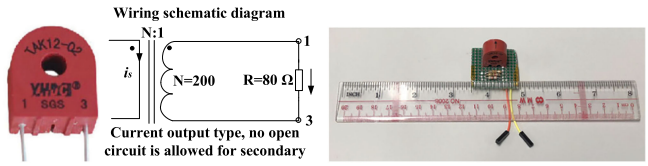

(a) (b)

Fig. 23. High-frequency pulse current sensor of TAK12-02 (a) Wiring schematic diagram. (b) Photograph of the pulse current sensor.

From (9), the mutual inductance can simply be expressed as

$$M = \frac{4V_{\text{in}} \sin\frac{\alpha}{2}}{\pi\omega i_{s\_\text{peak}}} \tag{42}$$

where i_{s_peak} is the peak of i_s. For $V_{\text{in}} = 78\,\text{V}$, the control angle α can be fixed at 0.48π, as shown in Fig. 13, leaving M inversely proportional to i_{s_peak}. The process of peak current detection is shown in Fig. 22 for the estimation of M. First, a signal copy of the secondary current i_s is sampled by a current sensor, with high-frequency components being filtered out by a band-pass filter. The phase is also corrected. Next, the zero-crossing time point of the signal is detected by an ultrafast amplifier. Finally, the zero-crossing time point is taken as a flag signal for a microcontroller, which after a time delay of one quarter (1/4) period, triggers an analog-to-digital module to digitize the peak current of i_s for the control of the converter.

A high frequency pulse current sensor shown in Fig. 23 is used to sample the secondary current i_s. The actual i_s and the measured v_{sensor} follow $v_{\text{sensor}} = \frac{i_s R}{N}$. In order to observe the estimation results directly, the estimated value of M inside DSP is converted to an analog signal by a digital-to-analog (DA) module. In this article, we adopt DAC8501E as the DA module to convert the estimated value into an analog signal v_{DA}.

Fig. 24(b) shows the transient experimental waveforms with the coupling coefficient changing from $k = 0.243$ to $k = 0.271$. Fig. 24(a) and (c) are corresponding steady-state waveforms under $k = 0.271$ and $k = 0.243$, respectively. It is clear that v_{sensor} can well track the secondary current i_s both in transient and steady state. The output of DA module, v_{DA}, can well track the peak envelope of v_{sensor}, which shows that our designed control strategy can well estimate the mutual inductance.

The proposed control strategy is validated under the aligned condition ($k = 0.252$) and two points of misaligned conditions ($k = 0.243$, $k = 0.271$). The efficiency is maintained at around 87.5% under all conditions, while the output power is kept at 120 W, as shown in Fig. 25. Therefore, the proposed optimal control strategy can still be readily implemented under a misaligned condition.

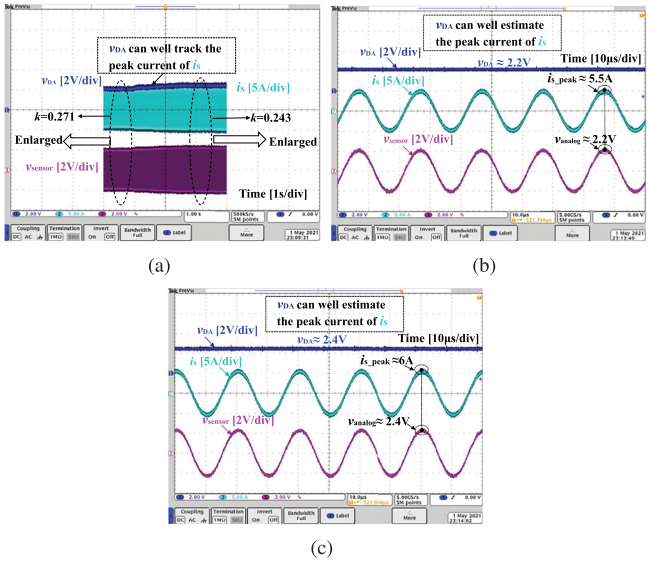

Fig. 24. Experimental waveforms of measured misalignment. (a) Transient waveforms of k changing from $k = 0.243$ to $k = 0.271$. (b) Steady-state waveforms at $k = 0.271$. (c) Steady-state waveforms at $k = 0.243$.

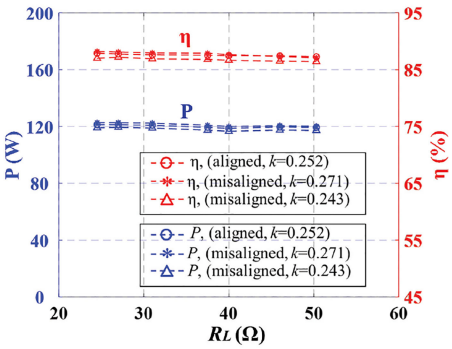

Fig. 25. Comparisons of measured charging powers and efficiencies when misalignment occurs.

D. Comparison of CP and CC Modes of Charging

The CP mode charging is proposed in this article as an alternative to the CC mode charging. The next phase CV charging is the same for the two charging profiles. A comparison of our proposed optimal CP mode charging and some reported efficiency optimization using the CC mode charging [19], [20] with the same topology will be given in this subsection. Here, in order to compare the charging power and charging time, two assumptions are made: (a) the battery voltage increases linearly during the CC mode charging, and (b) it takes 1 h to charge the battery from the cutoff voltage $V_{\min} = 55$ V to the predetermined voltage $V_{\max} = 78$ V using the CP mode charging. Therefore, with the rate power of $P_N = 120$ W, the battery capacity is $Q = 0.12$ kW·h. The charging current I_C under the CC mode charging should satisfy

$$I_C = \frac{Q}{\int_0^{1\,h} (55 + 23t)dt} \tag{43}$$

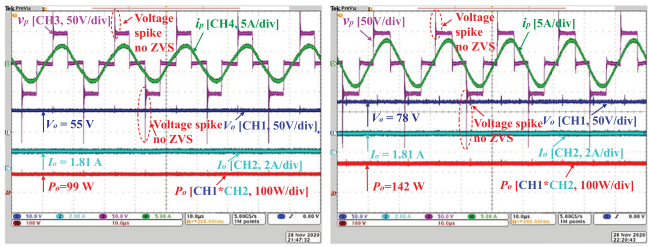

Fig. 26. Experimental steady-state operating waveforms of v_p, i_p, v_o, i_o, and P_o at (a) the start ($R_L = 25.2\,\Omega$) and (b) the end ($R_L = 50.7\,\Omega$) of the CC mode charging previously studied in [19].

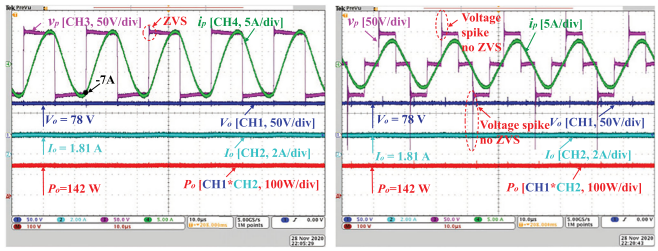

Fig. 27. Experimental steady-state operating waveforms of v_p, i_p, v_o, i_o, and P_o at (a) the start ($R_L = 25.2\,\Omega$) and (b) the end ($R_L = 50.7\,\Omega$) of CC mode charging previously studied in [20].

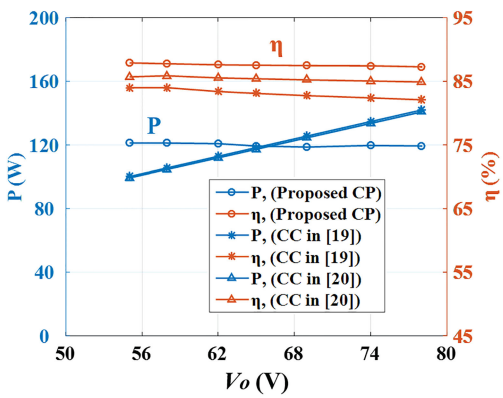

Fig. 28. Comparisons of experimental charging power and efficiency of the proposed CP mode of charging and the two implementations of optimal CC mode of charging [19], [20].

giving $I_C = 1.805$ A. Figs. 26 and 27 show the steady-state waveforms of $I_C = 1.805$ A with optimal CC charging strategies from start to end of the CC mode charging [19], [20]. The implementation shown in [19] cannot achieve ZVS as evidenced from the large voltage spikes during switching times. Moreover, the implementation given in [20] has large reactive circulating power as shown in the large negative current during switching times. Fig. 28 gives a comparison of measured charging powers and efficiencies, which show that the efficiency of our proposed CP mode charging is higher than that of the optimal CC mode of charging in [19] and [20].

Moreover, the maximum charging power of CC mode of charging is $P_{\max} = I_C * V_{\max} = 147$ W, which is larger than the rated power (120 W) of our CP mode of charging. Therefore,

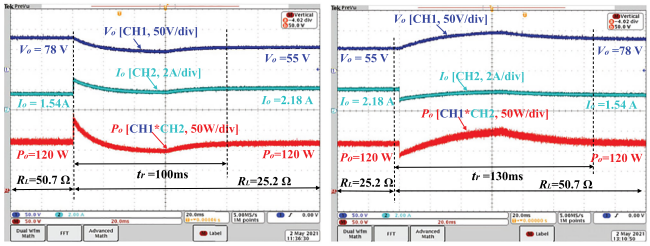

(a) (b)

Fig. 29. Dynamic waveforms of the IPT system using the proposed control strategy. (a) R_L steps from 50.7 to 25.2 Ω. (b) R_L steps from 25.2 to 50.7 Ω.

the CC mode of charging has a higher demand for the rating of heat sink. Alternatively, if the maximum charging power of CC mode is kept at 120 W, then, the charging current reduces to 1.538 A. According to (43), the charging time becomes 1.18 h, which is longer than 1 h. Therefore, CP mode of charging is more advantageous than the CC mode of charging.

E. Controller Speed in Response to Load Change

Step changes in the load are applied to examine the response of the controller. The waveforms of I_o, V_o and power $P_o = V_o * I_o$ under step changes of battery resistance R_L from 50.7 to 25.2 Ω and from 25.2 to 50.7 Ω are shown in Fig. 29. The response time t_r are 100 and 130 ms, respectively. It can be observed that P_o is kept constant at 120 W after duration t_r. These waveforms confirm that the system is stable.

F. Parameters Settings and Efficiency Performance

It should be noted that the parameters settings in this article are not designed for a certain target application. This article presents a general method of designing a fast and optimal CP charger for inductive power transfer. In practice, the input voltage, output voltage, and power rating of IPT chargers depend on the application scenarios. For example, the charging power and voltage range of the battery are determined for a certain type of EVs.

Moreover, under different input/output voltage or power settings, using the method provided in our article, an optimal strategy can be applied to different applications for achieving optimal efficiency. For example, for this specific prototype, keeping the charging power $P_N = 120$ W unchanged, if we set $V_{\text{in}} = 50$ V and $V_o = 50$ V, according to the solution steps of the optimal solution provided in this article, the optimal solutions are $\alpha = 0.74\pi$, $\beta = 0.74\pi$, and $\theta = 0.33\pi$ and the measured system efficiency is 90.2%. The efficiency performance can be improved further by using better components, such as the magnetic coupler with small resistances and MOSFETs with small ON-resistances.

VII. Conclusion

An optimal control strategy of a single-stage IPT battery charger has been proposed to achieve maximum efficiency for CP+ output. By controlling the conduction angles in the primary inverter, secondary active rectifier, and phase shift angle between the two sides properly, the system can achieve ZVS, minimum circulating power, and minimum overall losses simultaneously throughout the charging process. Compared with previously proposed constant-power chargers, PI controllers can be eliminated by virtue of the compensated overall losses model, saving cost and reducing design complexity. The proposed control strategy has been validated experimentally under misalignment conditions and load transients.

References

[1] A. Zaheer, H. Hao, G. A. Covic, and D. Kacprzak, "Investigation of multiple decoupled coil primary pad topologies in lumped IPT systems for interoperable electric vehicle charging," *IEEE Trans. Power Electron.*, vol. 30, no. 4, pp. 1937–1955, Apr. 2015.

[2] J. Yungtaek and M. M. Jovanovic, "A contactless electrical energy transmission system for portable-telephone battery chargers," *IEEE Trans. Ind. Electron.*, vol. 50, no. 3, pp. 520–527, Jun. 2003.

[3] S. Y. R. Hui and W. W. C. Ho, "A new generation of universal contactless battery charging platform for portable consumer electronic equipment," *IEEE Trans. Power Electron.*, vol. 20, no. 3, pp. 620–627, May 2005.

[4] N. M. Neihart and R. R. Harrison, "Micropower circuits for bidirectional wireless telemetry in neural recording applications," *IEEE Trans. Biomed. Eng.*, vol. 52, no. 11, pp. 1950–1959, Nov. 2005.

[5] Q. Chen, S. C. Wong, C. K. Tse, and X. Ruan, "Analysis, design, and control of a transcutaneous power regulator for artificial hearts," *IEEE Trans. Biomed. Circuit Syst.*, vol. 3, no. 1, pp. 23–31, Feb. 2009.

[6] J. H. Kim *et al.*, "Development of 1-MW inductive power transfer system for a high-speed train," *IEEE Trans. Ind. Electron.*, vol. 62, no. 10, pp. 6242–6250, Oct. 2015.

[7] S. Y. Choi, B. W. Gu, S. Y. Jeong, and C. T. Rim, "Advances in wireless power transfer systems for roadway-powered electric vehicles," *IEEE J. Emerg. Sel. Topics Power Electron.*, vol. 3, no. 1, pp. 18–36, Mar. 2015.

[8] Z. Bi, T. Kan, C. C. Mi, Y. Zhang, Z. Zhao, and G. A. Keoleian, "A review of wireless power transfer for electric vehicles: Prospects to enhance sustainable mobility," *Appl. Energy*, vol. 179, pp. 413–425, Oct. 2016.

[9] X. Qu, H. Han, S. C. Wong, C. K. Tse, and W. Chen, "Hybrid IPT topologies with constant current or constant voltage output for battery charging applications," *IEEE Trans. Power Electron.*, vol. 30, no. 11, pp. 6329–6337, Nov. 2015.

[10] J. Sallan, J. L. Villa, A. Llombart, and J. F. Sanz, "Optimal design of ICPT systems applied to electric vehicle battery charge," *IEEE Trans. Ind. Electron.*, vol. 56, no. 6, pp. 2140–2149, Jun. 2009.

[11] W. Zhang, S. C. Wong, C. K. Tse, and Q. Chen, "Design for efficiency optimization and voltage controllability of series-series compensated inductive power transfer systems," *IEEE Trans. Power Electron.*, vol. 29, no. 1, pp. 191–200, Jan. 2014.

[12] Z. Huang, S. C. Wong, and C. K. Tse, "Design of a single-stage inductive power-transfer converter for efficient EV battery charging," *IEEE Trans. Veh. Technol.*, vol. 66, no. 7, pp. 5808–5821, Jul. 2017.

[13] W. X. Zhong and S. Y. R. Hui, "Maximum energy efficiency tracking for wireless power transfer systems," *IEEE Trans. Power Electron.*, vol. 30, no. 7, pp. 4025–4034, Jul. 2015.

[14] Z. Huang, S. C. Wong, and C. K. Tse, "Control design for optimizing efficiency in inductive power transfer systems," *IEEE Trans. Power Electron.*, vol. 33, no. 5, pp. 4523–4534, May 2018.

[15] M. Fu, C. Ma, and X. Zhu, "A cascaded boost-buck converter for high efficiency wireless power transfer systems," *IEEE Trans. Ind. Inform.*, vol. 10, no. 3, pp. 1972–1980, Aug. 2014.

[16] R. Mai, Y. Liu, Y. Li, P. Yue, G. Cao, and Z. He, "An active-rectifier-based maximum efficiency tracking method using an additional measurement coil for wireless power transfer," *IEEE Trans. Power Electron.*, vol. 33, no. 1, pp. 716–728, Jan. 2018.

[17] B. Nguyen *et al.*, "An efficiency optimization scheme for bidirectional inductive power transfer systems," *IEEE Trans. Power Electron.*, vol. 30, no. 11, pp. 6310–6319, Nov. 2015.

[18] T. Diekhans and R. W. de Doncker, "A dual-side controlled inductive power transfer system optimized for large coupling factor variations and partial load," *IEEE Trans. Power Electron.*, vol. 30, no. 11, pp. 6320–6328, Nov. 2015.

[19] Z. Li, K. Song, J. Jiang, and C. Zhu, "Constant current charging and maximum efficiency tracking control scheme for supercapacitor wireless charging," *IEEE Trans. Power Electron.*, vol. 33, no. 10, pp. 9088–9100, Oct. 2018.
[20] Z. Huang, S. C. Wong, and C. K. Tse, "An inductive-power-transfer converter with high efficiency throughout battery-charging process," *IEEE Trans. Power Electron.*, vol. 34, no. 10, pp. 10245–10255, Oct. 2019.
[21] S. S. Zhang, "The effect of the charging protocol on the cycle life of a Li-ion battery," *J. Power Sources*, vol. 161, no. 7, pp. 1385–1391, Jul. 2006.
[22] Z. Huang, C. S. Lam, P. Mak, R. P. Martins, S. C. Wong, and C. K. Tse, "A single-stage inductive-power-transfer converter for constant-power and maximum-efficiency battery charging," *IEEE Trans. Power Electron.*, vol. 35, no. 9, pp. 8973–8984, Sep. 2020.
[23] Y. Jiang *et al.*, "Phase-locked loop combined with chained trigger mode used for impedance matching in wireless high power transfer," *IEEE Trans. Power Electron.*, vol. 35, no. 4, pp. 4272–4285, Apr. 2020.
[24] J. Zhang, J. Zhao, Y. Zhang, and F. Deng, "A wireless power transfer system with dual switch-controlled capacitors for efficiency optimization," *IEEE Trans. Power Electron.*, vol. 35, no. 6, pp. 6091–6101, Jun. 2020.
[25] U. K. Madawala and D. J. Thrimawithana, "A bidirectional inductive power interface for electric vehicles in V2G systems," *IEEE Trans. Power Electron.*, vol. 58, no. 10, pp. 4789–4796, Oct. 2011.
[26] A. A. S. Mohamed, A. Berzoy, and O. A. Mohammed, "Experimental validation of comprehensive steady-state analytical model of bidirectional WPT system in EVs applications," *IEEE Trans. Veh. Technol.*, vol. 66, no.7, pp. 5584–5594, Jul. 2017.
[27] H. Li, J. Fang, S. Chen, K. Wang, and Y. Tang, "Pulse density modulation for maximum efficiency point tracking of wireless power transfer systems," *IEEE Trans. Power Electron.*, vol. 33, no. 6, pp. 5492–5501, Jun. 2018.

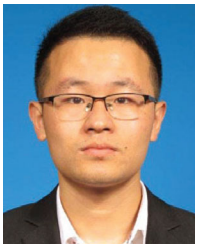

Fei Xu (Student Member, IEEE) received the B.Eng. degree in electrical engineering from China Agricultural University, Beijing, China, in 2016, and the M.Phil. degree from the Institute of Electrical Engineering, Chinese Academy of Sciences, Beijing, China, in 2019. He is currently working toward the Ph.D. degree with the Department of Electronic and Information Engineering, The Hong Kong Polytechnic University, Hong Kong.

His research interests include inductive power transfer and bidirectional dual-active-bridge dc–dc converter.

Siu-Chung Wong (Senior Member, IEEE) received the B.Sc. degree in physics from the University of Hong Kong, Hong Kong, in 1986, the M.Phil. degree in electronics from the Chinese University of Hong Kong, Hong Kong, in 1989, and the Ph.D. degree from the University of Southampton, Southampton, U.K., in 1997.

In 1988, he joined The Hong Kong Polytechnic University, Hong Kong, as an Assistant Lecturer. He is currently an Associate Professor with the Department of Electronic and Information Engineering, The Hong Kong Polytechnic University, Hong Kong, where he conducts research in power electronics. From 2012 to 2015, he was a Chutian Scholar Chair Professor with the Hubei Provincial Department of Education, China, and the appointment was hosted by the Wuhan University of Science and Technology, Wuhan, China. In 2013, he was a Guest Professor with the School of Electrical Engineering, Southeast University, Nanjing, China. He was a Visiting Scholar with the Center for Power Electronics Systems, Virginia Tech, VA, USA, in November 2008, Aero-Power Sci-Tech Center, Nanjing University of Aeronautics and Astronautics, Nanjing, China, in January 2009, and the School of Electrical Engineering, Southeast University, Nanjing, China, in March 2012.

Dr. Wong is a member of the Electrical College, Institution of Engineers, Australia. He is an Editor for the *Energy and Power Engineering Journal* and a Member of the Editorial Board of the *Journal of Electrical and Control Engineering*. He is a Guest Associate Editor for the IEEE JOURNAL OF EMERGING AND SELECTED TOPICS IN POWER ELECTRONICS, Special Issue on "Power Electronics for Biomedical Applications" in 2014, and an Associate Editor for the IEEE TRANSACTIONS ON CIRCUITS AND SYSTEMS II.

Chi K. Tse (Fellow, IEEE) received the B.Eng. (with first class hons.) degree with first class honors and the Ph.D. degrees from the University of Melbourne, Parkville, VIC, Australia, in 1987 and 1991, respectively, both in electrical engineering,.

He is currently the Chair Professor of Electrical Engineering with City University of Hong Kong, Hong Kong, and was Chair Professor and Head of Electronic and Information Engineering with Hong Kong Polytechnic University, Hong Kong. His research interests include power electronics, nonlinear systems, and complex network applications.

Dr. Tse was the recipient of a number of research and industry awards, including Prize Paper Awards by IEEE TRANSACTIONS ON POWER ELECTRONICS in 2001, 2015, and 2017, RISP Journal of Signal Processing Best Paper Award in 2014, Best paper Award by International Journal of Circuit Theory and Applications, in 2003, two Gold Medals at the International Inventions Exhibition in Geneva, in 2009 and 2013, a Grand Prize and Gold Medal at the Silicon Valley International Invention Festival, in 2019, and a number of recognitions by the academic and research communities, including honorary professorship by several Chinese and Australian universities, Chang Jiang Scholar Chair Professorship, IEEE Distinguished Lectureship, Distinguished Research Fellowship by the University of Calgary, Gledden Fellowship and International Distinguished Professorship-at-Large by the University of Western Australia. He serves and has served as Editor-in-Chief for the IEEE TRANSACTIONS ON CIRCUITS AND SYSTEMS II, from 2016 to 2019, *IEEE Circuits and Systems Magazine*, from 2012 to 2015, and IEEE CIRCUITS AND SYSTEMS SOCIETY NEWSLETTER (since 2007), Associate Editor for three IEEE Journal/Transactions, Editor for *International Journal of Circuit Theory and Applications*, and is on the Editorial Board of the IEEE PROCEEDINGS.